Article

Numerical Simulation of Proppant Transport in Major and Branching Fractures Based on CFD-DEM

Luo Zuo, Xiaolong Li, Zhongxi Han, Qing You, and Xiaoqiang Liu*

Read Online

ACCESS | 📊 Metrics & More | 📖 Article Recommendations

ABSTRACT: This research investigated the effect of branching fracture, proppant, and fracturing fluid on proppant transport based on the CFD-DEM coupling model. The obtained results show that the balance height of embankment in the major fracture decreases gradually with increasing angle between major and branching fractures, while it increases gradually in the branching fracture. This is because the additional resistance of fracturing fluid flow at the joint increases with increasing angle, leading to the decrease of the fracturing fluid velocity. The proppant is prone to settling in branching fractures, resulting in the increase of embankment height in the branching fracture. At angles of 45, 60, and 90°, as the diameter of the proppant increases from 0.8 to 1.1 mm, the balance height of embankment increases slightly in the major fracture, while it decreases in the branching fracture. The frictional resistance of the fracture wall enhances the difficulty of large proppant entering the branching fracture, resulting in a decrease in the amount of proppant entering the branching fracture and a decrease of the balance height of embankment in the branching fracture. In the low-viscosity fracturing fluid, the proppant quickly deposits at the bottom of the fracture as it enters the fracture. Improving the viscosity of the fracturing fluid can significantly enhance its ability to transport the proppant. The proppant is less likely to quickly settle in high-viscosity fracturing fluids, especially when the fracturing fluid viscosity exceeds 50 mPa·s.
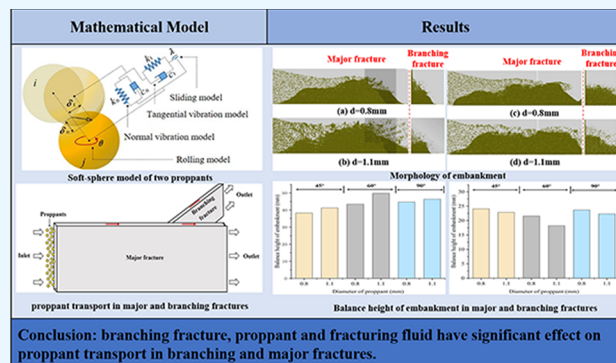
1. INTRODUCTION

Hydraulic fracturing is an important technology for developing low-permeability oil and gas reservoirs. The transport and placement of the proppant in fracturing fractures directly affects fracture conductivity, further affecting the productivity of oil and gas.[1−3] Clarifying proppant transport in fractures is of great significance for optimizing the fracturing design.

Proppant transport with the fracturing fluid in fractures is a typical solid−liquid two-phase flow.[4,5] At present, the main simulation methods are the Euler−Euler method and the Euler−Lagrange method. The Euler−Euler method treats the solid phase as a pseudo fluid, considers both liquid phase and solid phase as continuous media, and introduces porosity to characterize the relationship between the two phases. However, the proppant is considered a quasi-fluid phase, and the force between the proppant and the fracture wall is ignored.[6−11]

In the Euler−Lagrange method, the fluid is treated as a continuous phase and the proppant is treated as a discrete phase, which better reflects the actual situation. The motion of the fracturing fluid is modeled by using computational fluid dynamics (CFD). Based on the modified Navier−Stokes equation, the Euler method is used to solve the fluid flow field between the fluid and the solid.[12] Fluid is considered incompressible, which can reduce the computation while meeting the accuracy requirement.[13] As a discrete phase, the movement of the proppant is modeled using the discrete element method (DEM).[14] DEM uses damping force and inelastic contact force to accurately calculate the forces between particles and fracture walls.[15] DEM can consider the contact force and collision process between particles, calculate and track the trajectory of each proppant particle, and simulate the particle flow in the multiphase flow.[16] Newton's second law is applied to calculate the resultant force acting on a single proppant particle, including mass force, surface force, and fluid and other particle forces. The velocity and displacement changes of proppant particles are updated based on the resultant forces exerted on proppant particles. The size and direction of the contact force between the proppant particles are updated as well. Through the momentum exchange
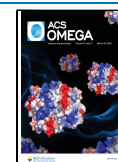
equation, CFD and DEM are coupled to simulate the transport of proppant in fractures.

Tomac and Gutierrez[17] used the CFD-DEM coupling model to simulate the transport of proppant in a single fracture. The results suggest that the size ratio between the proppant diameter and the fracture width significantly affects proppant transport. Wilson[18] used the Euler−Lagrange method to simulate proppant transport with slippery water. The effects of proppant density, proppant diameter, and injection rate on proppant transport are investigated. Blyton et al.[19] used the Euler−Lagrange method to study the influence of proppant diameter, proppant concentration, and fracture width on proppant transport. The ratio of the proppant diameter to the fracture width affects the relative velocity between solid and liquid phases. Blyton et al.[19,20] used the Euler−Lagrange method to study the interaction forces between proppant particles and fracture walls during proppant transport. They found that these forces can affect the formation of a sand embankment, which cannot be captured in the Euler−Euler method. At the same time, compared with the MP-PIC method, the Euler−Lagrange method has a greater computational complexity but higher accuracy. Zhang et al.[21,22] investigated the proppant transport in fracturing fractures of a horizontal well. Proppant accumulates near the wellbore to form a sand embankment and then migrates with the fracturing fluid to the far end of fractures. Rahman et al.[23] presented the hydraulic fracturing design optimization with free design variables, design constraints, and objective function.

At present, the research on proppant transport is mainly focused on the single hydraulic fracture. During hydraulic fracturing, in addition to forming the major fracture, a branching fracture is also formed. The fracturing fluid is diverted in the branching fracture, which inevitably affects proppant transport in major and branching fractures. Especially the low viscosity of slick water greatly reduces the sand carrying capacity. After the proppant enters the fracture, it is easy to settle and accumulate at the bottom, forming a sand embankment, which increases the difficulty of the proppant moving toward the branching fracture. Besides, current research typically simplifies the fracture wall to a smooth state, ignoring the influence of roughness on proppant migration and placement, while the rough fracture wall also affects the migration ability of proppants in major and branching fractures. In general, current research in this area is insufficient, and it is necessary to conduct research on proppant transport in major and branching fractures. This research conducted numerical simulation of proppant transport in major and branching fractures based on the CFD-DEM coupling model. Roughness of the fracture is considered. The effect of branching fracture, proppant, and fracturing fluid on proppant transport is investigated. The detailed research is introduced in the following sections.

2. MATHEMATICAL MODEL

2.1. CFD. Fracturing fluid flow is calculated by the CFD model, including fluid continuity equation, momentum equation, and turbulent equation.

2.1.1. Fluid Continuity Equation. As a fluid phase, fracturing fluid has independent continuous physical field parameters, such as velocity, concentration, and pressure. Proppants affect fluid flow, which is reflected by the volume fraction of the fracturing fluid and the momentum exchange

source between the fracturing fluid and proppants. The continuity equation of fracturing fluid is expressed as follows:[24]

$$\frac{\partial}{\partial t}(\alpha_f \rho_f) + \nabla \cdot (\alpha_f \rho_f \mathbf{u}_f) = 0 \tag{1}$$

$$\alpha_f = \frac{n_f}{N} \tag{2}$$

in which α_f is the fluid volume fraction, ρ_f is the fluid density, kg m^{-3}, $\mathbf{u}_f$ is the fluid velocity, m s^{-1}, and n_f is the number of fluid points in the grid unit. N is the total number of points in the grid unit.

2.1.2. Momentum Equation. Momentum equation is expressed as follows:

$$\frac{\partial}{\partial t}(\alpha_f \rho_f \mathbf{u}_f) + \nabla \cdot (\alpha_f \rho_f \mathbf{u}_f)$$
$$= -\alpha_f \nabla P + \nabla \cdot (\alpha_f \boldsymbol{\tau}_f) - + \alpha_f \rho_f \mathbf{g} + \mathbf{M}_{fs} \tag{3}$$

$$\boldsymbol{\tau}_f = \mu_f [(\nabla \mathbf{u}_f) + (\nabla \mathbf{u}_f{}^T)] \tag{4}$$

in which P is the fluid pressure, Pa. $\boldsymbol{\tau}_f$ is the fluid viscous stress tensor, N·m^{-2}. t is the time, s. $\mathbf{g}$ is the gravitational acceleration, m/s^2. $\mathbf{M}_{fs}$ is the momentum exchange source between the fluid and proppants, including collision force between proppants and interphase momentum transfer. μ_f is the dynamic viscosity of the fluid, Pa·s.

2.1.3. Turbulent Equation. With the continuous injection of fracturing fluid, proppants deposit at the bottom of the hydraulic fracture to form an embankment, reducing the space for fluid flow and increasing the fluid velocity. The nonuniformity of embankment surface also causes turbulence in the fracturing fluid. The strength of turbulence in the fracturing fluid can be expressed by the turbulence intensity as follows:[25]

$$I = \frac{u}{\overline{u}} = 0.16(\text{Re})^{-1/8} \tag{5}$$

$$\text{Re} = \frac{\rho_f U L}{\mu_f} \tag{6}$$

$$L = \frac{wH}{2(w + H)} \tag{7}$$

in which U is the average fluid velocity, m·s^{-1}. L is the characteristic length, m. Re is the Reynolds number. w is the width of hydraulic fracture, m. H is the height of hydraulic fracture, m.

In turbulent flow, there is a strong exchange of energy and momentum between proppants and fracturing fluid in the hydraulic fracture. $k-\varepsilon$ turbulent equation is used to calculate the turbulent kinetic energy and diffusion as follows:

$$\frac{\partial}{\partial t}(\rho k) + \frac{\partial}{\partial x_i}(\rho k u_i) = \frac{\partial}{\partial x_j}\left[\alpha_k \mu_{eff} \frac{\partial k}{\partial x_j}\right] + G_k - \rho \varepsilon \tag{8}$$

$$\frac{\partial(\rho \varepsilon)}{\partial t} + \frac{\partial(\rho \varepsilon u_i)}{\partial x_i}$$
$$= \frac{\partial}{\partial x_j}\left[\left(\mu + \frac{\mu_t}{\sigma_\varepsilon}\right)\frac{\partial \varepsilon}{\partial x_j}\right] + \rho C_1 E\varepsilon - \rho C_2 \frac{\varepsilon^2}{k + \sqrt{\nu\varepsilon}} \tag{9}$$

$$\begin{cases} \sigma_k = 1.0, \quad \sigma_\varepsilon = 1.2, \quad C_2 = 1.9 \\ C_1 = \max\left(0.43, \ \dfrac{\eta}{\eta + 5}\right) \\ \eta = (2E_{ij} \cdot E_{ij})^{1/2} \dfrac{k}{\varepsilon} \\ E_{ij} = \dfrac{1}{2}\left(\dfrac{\partial u_i}{\partial x_j} + \dfrac{\partial u_j}{\partial x_i}\right) \end{cases} \tag{10}$$

in which k is the turbulent kinetic energy, $m^2 \cdot s^{-2}$. ε is the turbulent dissipation rate, $m^2 \cdot s^{-3}$. σ_k and σ_ε are the corresponding Prandtl numbers for turbulent kinetic energy and turbulent dissipation rate, respectively. G_k is the turbulent kinetic energy caused by the average velocity, $kg \cdot m^{-2} \cdot s^2$. μ is the viscosity increment caused by turbulence, $Pa \cdot s$.

2.2. DEM. The proppant in the fracturing fluid is a discontinuous phase. DEM is suitable for solving mechanical problems in discontinuous media.[26]

In DEM, the movement of proppants is governed by Newton's second law. The displacement and angular velocity of the proppants are updated in each time step. The resultant torque of proppant collisions is calculated using the soft sphere model. The movement equation of the single proppant is expressed as follows:

$$m_p \frac{d\mathbf{u}_p}{dt} = \mathbf{F}_C + \mathbf{F}_A + \mathbf{F}_V \tag{11}$$

$$I_{pc} \frac{d\omega_p}{dt} = \mathbf{T}_{pc} \tag{12}$$

in which, m_p is the mass of the proppant, kg. $\mathbf{u}_p$ is the linear velocity of the proppant, $m \cdot s^{-1}$. $\mathbf{F}_C$ is the resultant force of proppant collision, N. $\mathbf{F}_A$ is the action force of the fluid on the proppant, N. $\mathbf{F}_V$ is the self-weight of the proppant, N. I_{pc} is the moment of inertia of the proppant, $kg \cdot m^2$. ω_p is the angular velocity of the proppant, $rad \cdot s^{-1}$. $\mathbf{T}_{pc}$ is the contact moment of force generated by the contact between proppants, $N \cdot m$.

Volume force is related to particle density including gravity and inertia force. Volume force is equivalent to the force on the the proppant center of mass.[27]

$$\mathbf{F}_V = \mathbf{F}_z + \mathbf{F}_p \tag{13}$$

in which $\mathbf{F}_z$ is the gravity of the proppant, N. $\mathbf{F}_p$ is the inertial force, N.

The force of fluid on the proppants is mainly reflected in the drag force and lifting force as follows.

$$\mathbf{F}_A = \mathbf{F}_d + \mathbf{F}_l \tag{14}$$

$$\mathbf{M}_{fs} = \mathbf{M}_{sf} \tag{15}$$

in which $\mathbf{F}_d$ is the fluid drag force, N. $\mathbf{F}_l$ is the fluid lift force, N. $\mathbf{M}_{sf}$ is the torque on proppants, $N \cdot m$.

Resultant force and force moment generated by the collision between particles are as follows:[28]

$$\mathbf{F}_C = \mathbf{F}_{c,n} + \mathbf{F}_{c,t} \tag{16}$$

$$\mathbf{M}_C = d_p \mathbf{F}_{c,t}/2 \tag{17}$$

in which, d_p is the proppant diameter, mm. $\mathbf{F}_{c,n}$ is the normal contact force, N. $\mathbf{F}_{c,t}$ is the tangential contact force, N.

The normal and tangential collision forces between proppants are equivalent to the resultant moments on the proppants' center of mass.[28]

$$\mathbf{F}_C = \mathbf{F}_{c,n} + \mathbf{F}_{c,t} \tag{18}$$

$$\mathbf{M}_C = d_p \mathbf{F}_{c,t}/2 \tag{19}$$

in which, d_p is the proppant diameter, mm. $\mathbf{F}_{c,n}$ is the normal contact force, N. $\mathbf{F}_{c,t}$ is the tangential contact force, N.

In DEM, the contact model is used to calculate the forces between proppants and the influence on proppant movement. There are two kinds of contact models in DEM, the hard sphere model and the soft sphere model. The hard sphere model refers to the plastic deformation of proppants being small and the duration being short when proppants contact. It is generally considered an immediate rebound after an instant collision, while in the soft sphere model, multiple proppants can be contacted at the same time, and partial overlap between proppants is allowed (as shown in Figure 1). It can describe
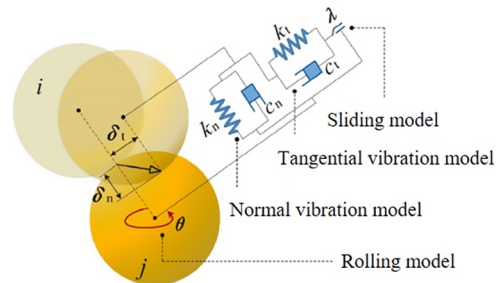

Figure 1. Soft sphere model of two proppants in contact with each other.

the changes of proppants in the whole process from contact to separation, and the contact time between the proppants is long. Due to the influence of multiple proppants contact on proppant movement, this study adopts the soft sphere model to calculate the contact force as follows.

$$\mathbf{F}_{c,n} = -k_n \delta_n^{3/2} \mathbf{n} - c_n \mathbf{u}_{p,n} \tag{20}$$

$$\mathbf{F}_{c,t} = -k_t \delta_t \mathbf{n} - c_t \mathbf{u}_{p,t} \tag{21}$$

in which, $\mathbf{F}_{c,n}$ and $\mathbf{F}_{c,t}$ are the normal and tangential contact forces, respectively. k_n and k_t are the normal and tangential stiffness coefficients, respectively. δ_n and δ_t are the normal and tangential overlap distances between colliding particles, respectively, mm. $\mathbf{n}$ is the normal unit vector between the contacting particles. c_n and c_t are the normal and tangential damping coefficients, respectively. $\mathbf{u}_{p,n}$ and $\mathbf{u}_{p,t}$ are the normal and tangential velocities, respectively, $m \cdot s^{-1}$.

2.3. Characterization Parameters of Embankment. Proppants settled in the hydraulic fracture form an embankment. The morphology of the embankment obviously affects the conductivity of the hydraulic fracture. It is necessary to put forward the corresponding characterization parameters to evaluate the embankment. In this section, the balance height of the embankment and the variance of embankment height are proposed as follows.

2.3.1. Balance Height of Embankment. Proppants settled in the hydraulic fracture reduce the fluid flow space, resulting in the increase of fluid velocity. When the fluid velocity increases to a threshold, the settlement and movement of
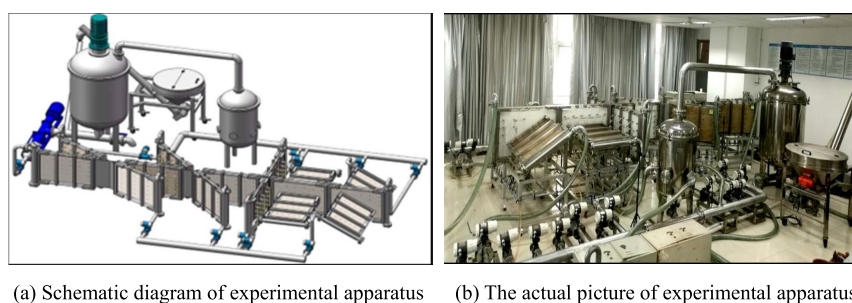
(a) Schematic diagram of experimental apparatus   (b) The actual picture of experimental apparatus

Figure 2. Experimental apparatus.

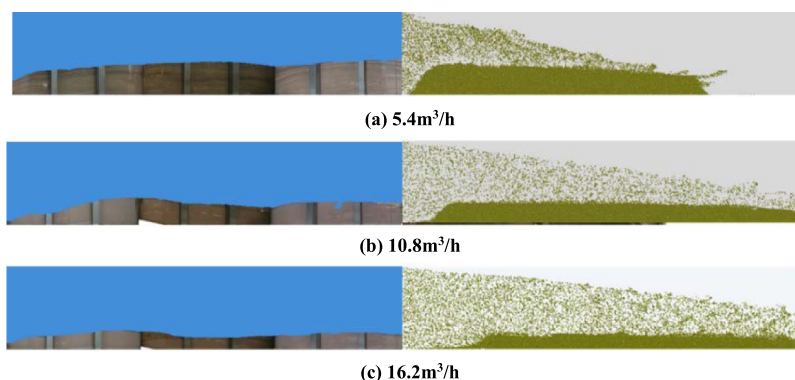
(a) 5.4m³/h

(b) 10.8m³/h

(c) 16.2m³/h

Figure 3. Morphology of proppant embankment: left is the experimental result and right is the numerical result.

proppants reach a dynamic balance, and the embankment height does not change, which is defined as the balance height of embankment as follows:

$$H_{EQ} = H_0 - h_{EQ} = H_0 - \frac{Q}{wv_{EQ}} \quad (22)$$

$$v_{EQ} = \frac{Q}{wh_{EQ}} \quad (23)$$

in which, H_{EQ} is the balance height of embankment, m. H_0 is the fracture height at balance, m. h_{EQ} is the height of fluid flow cross-section at balance, m. Q is the injection rate, m³·s⁻¹. w is the fracture width, m. v_{EQ} is the fluid velocity at balance, m·s⁻¹.

2.3.2. Variance of Embankment Height. The variance of embankment height represents the uniformity of proppant settlement, which is expressed as follows.

$$\sigma^2 = \frac{\Sigma(h_i - \bar{H})^2}{N} \quad (24)$$

in which σ^2 is the variance of embankment height, m². h_i is the embankment height of the target point at different locations, m. $\bar{H}$ is the average height of embankment, m. N is the number of target points.

3. MODEL VALIDATION

To verify the accuracy of the mathematical model, a lab experiment of proppant transport in a single fracture was performed based on a custom-made experimental apparatus (Figure 2). The apparatus has one major fracture with a length of 5m, a width of 5 mm, and a height of 720 mm. Branching fractures are connected with the major fracture, and the contact angle can be adjusted among 30, 45, 90, 135, and 150°. Filtration holes are added in this apparatus to simulate fracturing fluid filtration. Rough fracture surface is simulated by

sticking sand. The experimental parameters were set as follows: sand ratio of 5%, sand diameter of 30−50 mesh, fracturing fluid viscosity of 1 mPa·s, and fluid injection rate of 5.4, 10.8, and 16.2 m³/h, respectively. Numerical simulation was conducted using the same parameters as the experiment, and the morphology of proppant embankment was compared with the experimental results, as shown in Figures 3 and 4 and Table 1.

Figure 3 shows that the morphologies of proppant transport in the numerical and experimental results are similar. Figure 4 further proves that the balance height of the embankment and the volume ratio of proppant to fracture are consistent in numerical and experimental results. The above results indicate
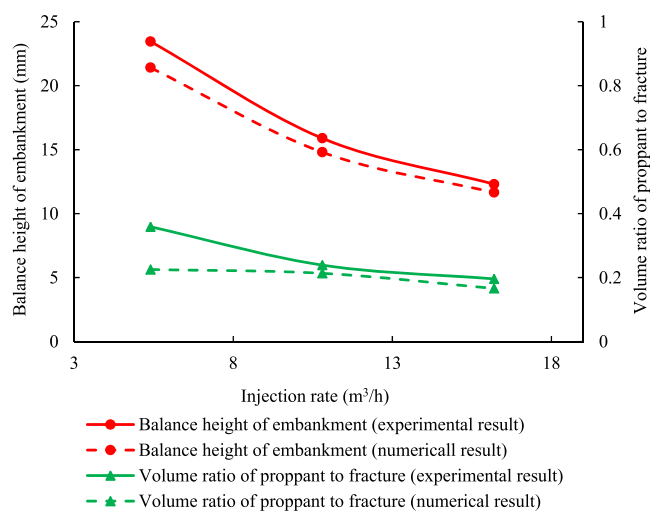

Figure 4. Comparison of the numerical result and experimental result.

Table 1. Numerical and Experimental Results of Proppant Transport

injection rate m³/h	balance height of embankment		volume ratio of proppant to fracture	
	experimental result/cm	numerical result/mm	experimental result/cm	numerical result/mm
5.4	23.45	21.41	0.359	0.2255
10.8	15.89	14.8	0.239	0.2136
16.2	12.3	11.65	0.196	0.1662

that the mathematical model can predict experimental results well, and the model proposed in this research is trustworthy.

4. PROPPANT TRANSPORT IN MAJOR AND BRANCHING FRACTURES

4.1. Model Description. A geometric model with major fracture and branching fracture is established, as shown in Figure 5. The size of the major fracture is $300 \times 60 \times 5$ mm, and the size of the branching fracture is $100 \times 60 \times 5$ mm. The branching fracture is located at two-thirds of the major fracture. The proppant is injected through the inlet of the major fracture, transported and settled in major and branching fractures, and then flows out from the outlet. The inlet boundary condition is the constant injection rate. The outlet boundary condition is constant pressure. Non slip boundaries are applied to the fracture surface to prevent displacement, and the velocity of the fracturing fluid at the fracture surface is zero. Other parameters are listed in Table 2.

4.2. Result and Analysis. *4.2.1. Angle between Major and Branching Fractures.* When the angle between the major fracture and the branching fracture is 15, 30, 45, 60, and 90°, the movement of the proppant in fractures is simulated. Simulated results are presented in Figures 6−8 and Table 3.

Figure 6 shows the morphology of embankments in the major fracture and branching fracture. With increasing angle between major and branching fractures, the balance height of embankment in the major fracture decreases gradually, while it increases gradually in the branching fracture (Figure 7).

This is because when the angle is small, the additional resistance at the joint of branching fracture and major fracture is low, and the fracturing fluid velocity is relatively high. The proppant carried by the fracturing fluid easily enters and passes through the branching fracture, making it difficult for the proppant to settle in the branching fracture. As the angle gradually increases, the additional resistance of the fracturing fluid flow at the joint increases, leading to a decrease of the fracturing fluid velocity. Proppant is prone to settling in the

Table 2. Parameters of Numerical Model

material	parameter	value
proppant	diameter/mm	0.4
	initial velocity/(m/s)	1
	density/(kg/m³)	2650
	Poisson's ratio	0.2
	shear modulus (MPa)	25
fracturing fluid	initial velocity/(m/s)	1
	viscosity/mPa·s	1
fracture wall	density/(kg/m³)	3000
	Poisson's ratio	0.23
	shear modulus (MPa)	100
	roughness (fractal dimension)	2.2
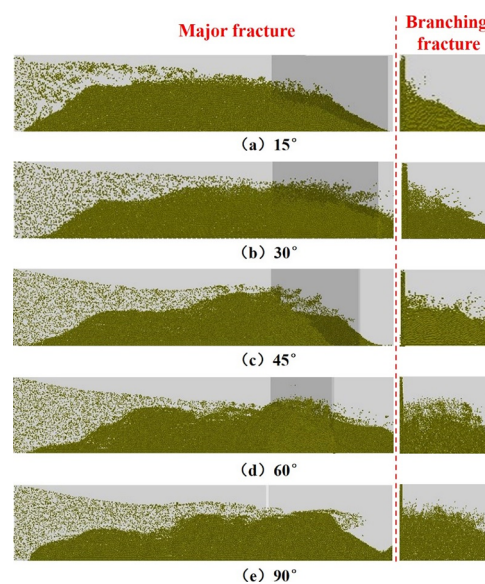
Figure 6. Morphology of embankment with different angles.

Table 3. Simulated Results of Embankment Height in Major and Branching Fractures

angle/°	balance height of embankment/mm		variance of embankment height/mm²	
	major fracture	branching fracture	major fracture	branching fracture
15	47.58	24.75	177.21	85.72
30	46.25	27.48	139.57	17.38
45	45.58	27.96	138.29	68.29
60	45.12	30.24	165.79	42.74
90	44.68	30.89	173.78	21.62
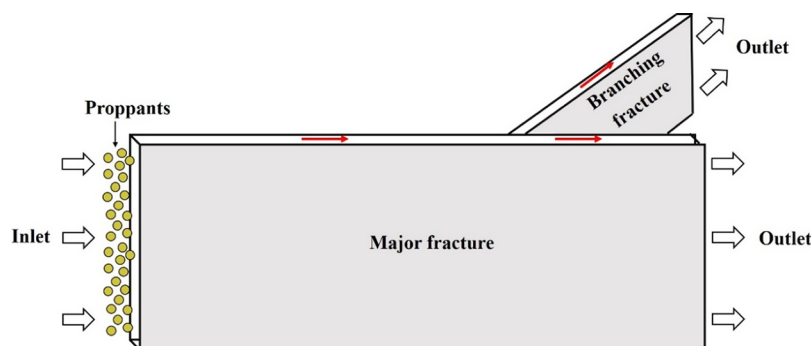
Figure 5. Schematic diagram of proppant transport in major and branching fractures.
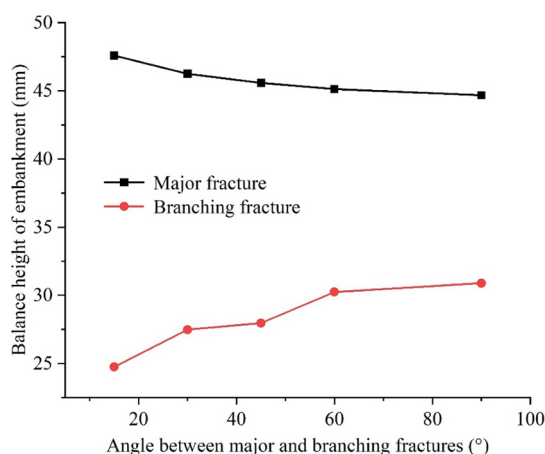
Figure 7. Balance height of embankment in major and branching fractures.

branching fracture, resulting in the increase of embankment height in the branching fracture. When the angle is 90°, the balance height of the embankment in the branching fracture is the largest.

Figure 8 shows the variance of embankment height in the major fracture and branching fracture. The variance of
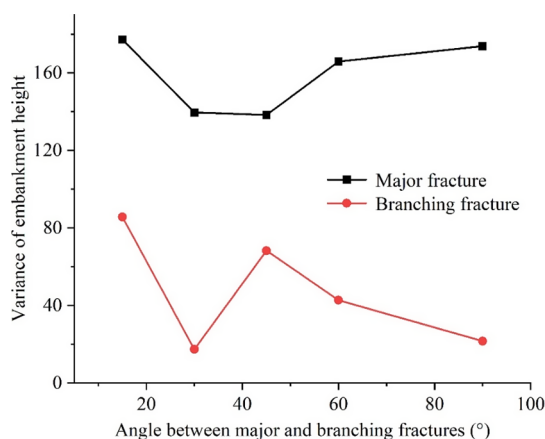

Figure 8. Variance of embankment height in major and branching fractures.

embankment height reaches the highest point in both major fracture and branching fracture when the angle is 15°. This is because the velocity of the fracturing fluid and the proppant movement is relatively high in this case, causing uneven placement of the proppant in both major and branching fractures.

The variance of embankment height in major fractures increases when the angle rises from 15 to 90°. As the angle increases, the flow resistance at the joint increases and the flow velocity decreases. This is because the increase of angle causes a change in the fracturing fluid velocity. The violent change of fluid velocity has a significant effect on the distribution of embankment morphology, resulting in increasing variance of embankment height in the major fracture, while the variance of embankment height in the branching fracture decreases when the angle rises from 45 to 90°. Because the fracturing fluid velocity in the branching fracture is small with a large angle, the proppant settlement and placement are relatively uniform.

4.2.2. Diameter of Proppant. The movement of proppant with the diameter of 0.8 mm and 1.1 mm is simulated when the angle between major and branching fracture is 45, 60, and 90°. Simulated results are presented in Figures 9−11.
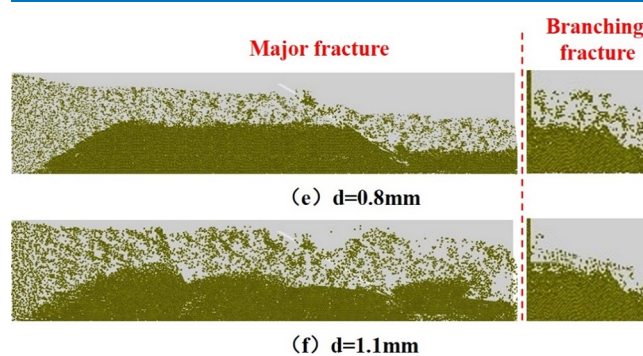

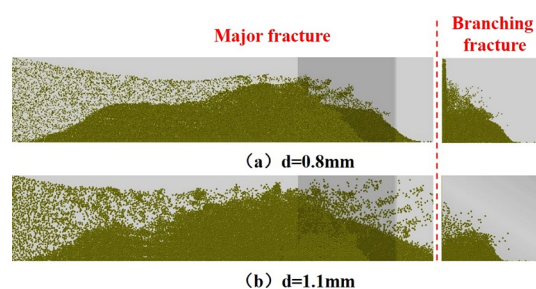**Figure 9.** Morphology of embankment with an angle of 45°.

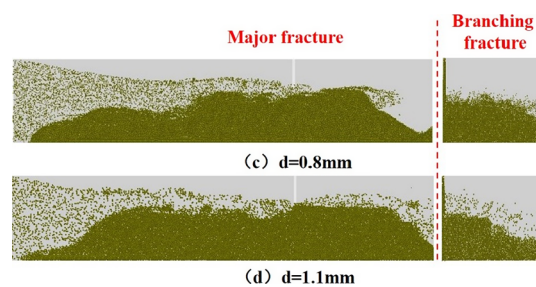**Figure 10.** Morphology of embankment with an angle of 60°.

Figure 11. Morphology of embankment with an angle of 90°

At angles of 45, 60, and 90°, as the diameter of the proppant increases from 0.8 to 1.1 mm, the balance height of embankment increases slightly in the major fracture, while it decreases in the branching fracture (Figures 12 and 13). According to Stokes formula,[29] the settling velocity of a solid particle is proportional to the square of its diameter. Therefore, the increase of proppant diameter accelerates its settlement in fracture. As the height of the embankment increases rapidly, the space for fluid flow in major fractures is restricted. Subsequent proppant prefers to settle near the entrance, causing the placement of embankment to move toward the entrance as a whole. This further accelerates the growth of embankment height until the fracturing fluid velocity reaches equilibrium velocity.

However, the balance height of embankment in the branching fracture decreases with increasing diameter of the proppant. Due to the small width of the branching fracture, the increasing diameter of the proppant enhances the influence of fracture wall on proppant movement. The frictional resistance
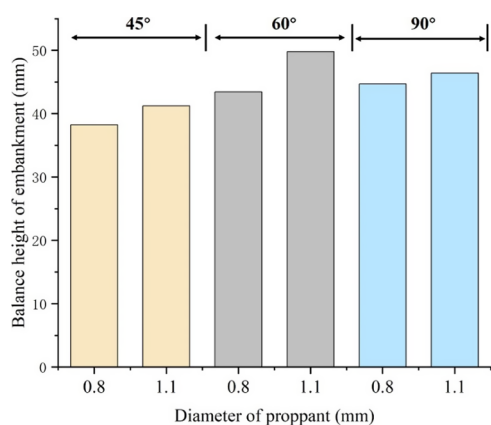
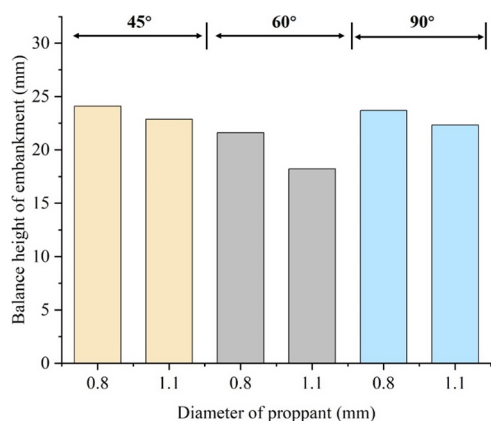**Figure 12.** Balance height of embankment in the major fracture.

Figure 13. Balance height of embankment in the branching fracture.

Figure 15. Balance height of embankment in major and branching fractures.

of fracture wall enhances the difficulty of a large proppant entering the branching fracture, resulting in a decrease in the amount of proppant entering the branching fracture and a decrease of the balance height of embankment in the branching fracture.

4.2.3. Viscosity of Fracturing Fluid. When the viscosity of the fracturing fluid is 1, 10, and 50 mPa·s, proppant transport in major and branching fractures is simulated, as shown in Figures 14 and 15.

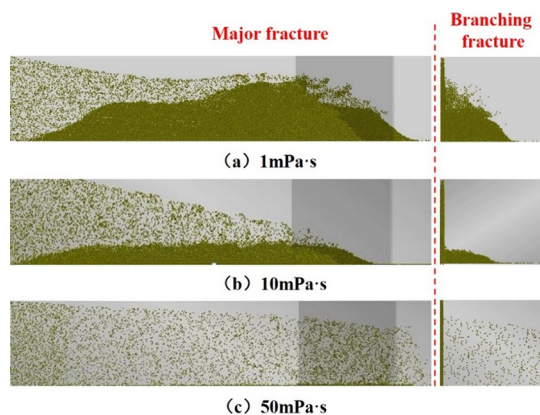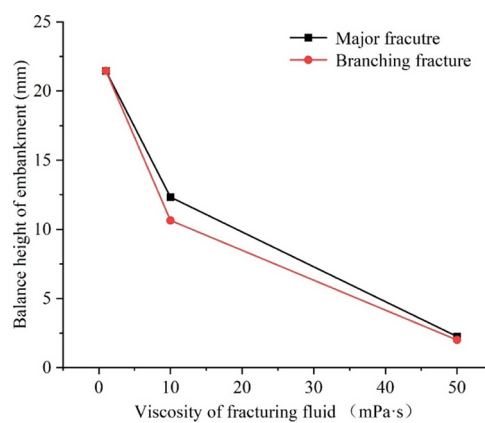As the viscosity of the fracturing fluid increases, the balance height of embankment in both major fracture and branching fracture significantly decreases. In low-viscosity fracturing fluid, the proppant quickly deposits at the bottom of the fracture as it enters the fracture. With the continuous deposition of proppant particles, the height of the embankment rises rapidly. Improving the viscosity of the fracturing fluid can significantly enhance its ability to transport the proppant. The proppant is less likely to quickly settle in high-viscosity fracturing fluids, especially when the fracturing fluid viscosity exceeds 50 mPa·s, as shown in Figure 14c.

5. CONCLUSIONS

1. With increasing angle between major and branching fractures, the balance height of embankment in the major fracture decreases gradually, while it increases gradually in the branching fracture. This is because the additional resistance of fracturing fluid flow at the joint increases with increasing angle, leading to the decrease of the fracturing fluid velocity. Proppant is prone to settling in the branching fracture, resulting in the increase of embankment height in the branching fracture.

2. At angles of 45, 60, and 90°, as the diameter of the proppant increases from 0.8 to 1.1 mm, the balance height of embankment increases slightly in the major fracture, while it decreases in the branching fracture. The frictional resistance of fracture wall enhances the difficulty of the large proppant entering the branching fracture, resulting in a decrease in the amount of proppant entering the branching fracture and a decrease of the balance height of embankment in the branching fracture.

3. In the low-viscosity fracturing fluid, the proppant quickly deposits at the bottom of the fracture as it enters the fracture. Improving the viscosity of the fracturing fluid can significantly enhance its ability to transport the proppant. The proppant is less likely to quickly settle in high-viscosity fracturing fluids, especially when the fracturing fluid viscosity exceeds 50 mPa·s.

Figure 14. Morphology of embankment with different fluid viscosities.

■ AUTHOR INFORMATION

Corresponding Author

Xiaoqiang Liu − *School of Energy Resources, China University of Geosciences Beijing, Beijing 100083, China; School of Earth and Space Sciences, Peking University, Beijing 100871,*

China; ⊙ orcid.org/0000-0001-5694-5976;
Email: liuxiaoqiang0535@126.com

Authors

Luo Zuo − *State Key Laboratory of Shale Oil and Gas Enrichment Mechanisms and Effective Development, Beijing 102206, China; SINOPEC Research Institute of Petroleum Engineering Co., Ltd., Beijing 100083, China*

Xiaolong Li − *SINOPEC Petroleum Exploration and Production Research Institute, Beijing 100083, China*

Zhongxi Han − *China Research Institute of Petroleum Exploration and Development, Beijing 100083, China*

Qing You − *School of Energy Resources, China University of Geosciences Beijing, Beijing 100083, China;* ⊙ orcid.org/0000-0002-0959-9502

Complete contact information is available at:
https://pubs.acs.org/10.1021/acsomega.3c09710

Notes

The authors declare no competing financial interest.

■ NOMENCLATURE

α_f fluid volume fraction
c_n normal damping coefficient
$\mathbf{F}_A$ action force of fluid on proppant, N
$\mathbf{F}_d$ fluid drag force, N
$\mathbf{F}_V$ self-weight of the proppant, N
$\mathbf{F}_P$ inertial force, N
$\mathbf{F}_{c,n}$ normal contact force, N
H height of hydraulic fracture, m
H_0 fracture height at balance, m
$\bar{H}$ average height of embankment, m
I_{pc} moment of inertia of proppant, kg·m^2
k turbulent kinetic energy, m^2·s^{-2}
k_t tangential stiffness coefficient
$\mathbf{M}_{sf}$ torque on proppants, N·m
m_p mass of proppant, kg
n_f number of fluid points in the grid unit
N number of target point
Q injection rate, m^3·s^{-1}
t time, s
$\mathbf{T}_{pc}$ contact moment of force generated by contact between proppants, N·m
$\mathbf{u}_f$ fluid velocity, m·s^{-1}
$\mathbf{u}_{p,n}$ normal velocity, m·s^{-1}
v_{EQ} fluid velocity at balance, m·s^{-1}
ω_p angular velocity of proppant, rad·s^{-1}
μ_f dynamic viscosity of fluid, Pa·s
σ_k Prandtl numbers for turbulent kinetic energy
σ_ε Prandtl numbers for turbulent dissipation rate
ε turbulent dissipation rate, m^2·s^{-3}
d_p proppant diameter, mm
c_t tangential damping coefficient
$\mathbf{F}_C$ resultant force of proppant collision, N
$\mathbf{F}_l$ fluid lift force, N
$\mathbf{F}_z$ gravity of proppant, N
$\mathbf{F}_{c,t}$ tangential contact force, N

$\mathbf{g}$ gravitational acceleration, m/s^2
G_k turbulent kinetic energy caused by average velocity, kg·m^{-2}·s^2
H_{EQ} balance height of embankment, m
h_i embankment height of target point at different locations, m
h_{EQ} height of fluid flow cross-section at balance, m
k_n normal stiffness coefficient
L characteristic length, m
$\mathbf{M}_{fs}$ momentum exchange source between the fluid and proppants
N total number of points in the grid unit
$\mathbf{n}$ normal unit vector between contacting particles
P fluid pressure, Pa
Re   Reynolds number
τ_f fluid viscous stress tensor, N·m^{-2}
U average fluid velocity, m·s^{-1}
$\mathbf{u}_p$ linear velocity of proppant, m·s^{-1}
$\mathbf{u}_{p,t}$ tangential velocity, m·s^{-1}
w width of hydraulic fracture, m
ρ_f fluid density, kg·m^{-3}
μ viscosity increment caused by turbulence, Pa·s
δ_n normal overlap distances between colliding particle, mm
δ_t tangential overlap distances between colliding particle, mm
σ^2 variance of embankment height, m^2

■ REFERENCES

(1) Abdelaziz, A.; Ha, J.; Li, M.; Magsipoc, E.; Sun, L.; Grasselli, G. Understanding hydraulic fracture mechanisms: From the laboratory to numerical modelling. *Advances in Geo-energy Research* **2023**, *7* (1), 66−68.

(2) He, J. C.; Zhang, K. S.; Liu, H. B.; Tang, M. R.; Zhang, X. L.; Zhang, G. Q. Laboratory investigation on hydraulic fracture propagation in sandstone-mudstone-shale layers. *Pet. Sci.* **2022**, *19* (4), 1664−1673.

(3) Hui, G.; Chen, Z. X.; Chen, S. N.; Gu, F. Hydraulic fracturing-induced seismicity characterization through coupled modeling of stress and fracture-fault systems. *Advances in Geo-energy Research* **2022**, *6* (3), 269−270.

(4) Dayan, A.; Stracener, S. M.; Clark, P. E. Proppant transport in slickwater fracturing of shale-gas formations. In *SPE Annual Technical Conference and Exhibition?*; SPE, 2009, SPE-125068.

(5) Guo, T. K.; Luo, Z. L.; Zhou, J.; Gong, Y. Z.; Dai, C. L.; Tang, J.; Yu, Y.; Xiao, B.; Niu, B. L.; Ge, J. J. Numerical simulation on proppant migration and placement within the rough and complex fractures. *Petroleum Science* **2022**, *19* (5), 2268−2283.

(6) Sahai, R. R.; Miskimins, J. L.; Olson, K. E. Laboratory results of proppant transport in complex fracture systems. In *SPE Hydraulic Fracturing Technology Conference*; OnePetro, 2014, SPE168579.

(7) Li, N.; Li, J.; Zhao, L., et al. Laboratory Testing and numeric simulation on laws of proppant transport in complex fracture systems. In *SPE Asia Pacific Hydraulic Fracturing Conference*; OnePetro, 2016, SPE181822.

(8) Tong, S.; Mohanty, K. K. Proppant transport study in fractures with intersections. *Fuel* **2016**, *181*, 463−477.

(9) Gu, M.; Mohanty, K. K. Effect of foam quality on effectiveness of hydraulic fracturing in shales. *International Journal of Rock Mechanics & Mining Sciences* **2014**, *70*, 273−285.

(10) Kong, X.; Mcandrew, J.; Cisternas, P. CFD study of using foam fracturing fluid for proppant transport in hydraulic fractures. In *Abu Dhabi International Petroleum Exhibition & Conference*; OnePetro, 2016.

(11) Crespo, F.; Aven, N. K.; Cortez, J., et al. Proppant distribution in multistage hydraulic fractured wells: a large-scale inside-casing

investigation. In *SPE hydraulic fracturing technology conference*; OnePetro, 2013, SPE163856.

(12) Shiozawa, S.; Mcclure, M. Comparison of pseudo-3D and fully-3D simulations of proppant transport in hydraulic fractures, including gravitational settling, formation of proppant banks, tip-screen out, and fracture closure. In *Paper presented at the SPE Hydraulic Fracturing Technology Conference, The Woodlands, Texas, USA*; OnePetro, 2016, SPE179132.

(13) Han, J.; Yuan, P.; Huang, X., et al. Numerical study of proppant transport in complex fracture geometry. In *SPE Rocky Mountain Petroleum Technology Conference/Low-Permeability Reservoirs Symposium*; SPE, 2016, SPE180243.

(14) Tomac, I.; Gutierrez, M. Fluid lubrication effects on particle flow and transport in a channel. *International Journal of Multiphase Flow* **2014**, *65*, 143−156.

(15) Tsuji, Y.; Kawaguchi, T.; Tanaka, T. Discrete particle simulation of two-dimensional fluidized bed. *Powder Technol.* **1993**, *77* (01), 79−87.

(16) Patankar, N. A.; Singh, P.; Joseph, D. D.; et al. A new formulation of the distributed Lagrange multiplier/fictitious domain method for particulate flows. *International Journal of Multiphase Flow* **2000**, *26* (09), 1509−1524.

(17) Tomac, I.; Gutierrez, M. Discrete element modeling of non-linear submerged particle collisions. *Granular Matter* **2013**, *15* (06), 759−769.

(18) Wilson, A. Unconventional proppant combined with channel fracturing increases effectiveness. *J. Pet. Technol.* **2015**, *67* (03), 89−93.

(19) Blyton, C. A.; Gala, D. P.; Sharma, M. M. A comprehensive study of proppant transport in hydraulic fracture. In *SPE Annual Technical Conference and Exhibition*; OnePetro, 2015, SPE174973.

(20) Tsai, K.; Fonseca, E.; Degaleesan, S.; et al. Advanced computational modeling of proppant settling in water fractures for shale gas production. *SPE J.* **2012**, *18* (01), 50−56.

(21) Zhang, G.; Li, M.; Gutierrez, M. Simulation of the transport and placement of multi-sized proppant in hydraulic fractures using a coupled CFD-DEM approach. *Advanced Powder Technology* **2017**, *28* (07), 1704−1718.

(22) Zhang, G.; Gutierrez, M.; Li, M. A coupled CFD-DEM approach to model particle-fluid mixture transport between two parallel plates to improve understanding of proppant micromechanics in hydraulic fractures. *Powder Technol. Systems* **2017**, *308*, 235−248.

(23) Rahman, M. M.; Rahman, M. K.; Rahman, S. S. Multicriteria hydraulic fracturing optimization for reservoir stimulation. *Petroleum Science and Technology* **2003**, *21* (11−12), 1721−1758.

(24) Shao, B.; Yan, Y. F.; Bi, C. F.; et al. Migration of irregular cuttings particles in big size by CFD-DEM coupled simulation model. *Sci. Technol. Eng.* **2017**, *27* (17), 190−195.

(25) Favier, J. *Industrial application of DEM: opportunities and challenges*; DEM Solutions Ltd., 2008.

(26) Cundall, P. A.; Strack, O. D. L. Discussion: A discrete numerical model for granular assemblies. *Géotechnique* **1980**, *30* (03), 331−336.

(27) Chaudhuri, B.; Muzzio, F. J.; Tomassone, M. S. Modeling of heat transfer in granular flow in rotating vessels. *Chem. Eng. Sci.* **2006**, *61* (19), 6348−6360.

(28) Michael, M.; Vogel, F.; Peters, B. DEM-FEM coupling simulations of the interactions between a tire tread and granular terrain. *Computer Methods in Applied Mechanics and Engineering* **2015**, *289* (01), 227−248.

(29) Constantin, P. An Eulerian-Lagrangian Approach to the Navier-Stokes Equations. *Communications in Mathematical Physics* **2001**, *216* (3), 663−686.